

Lateral migration of flexible fibers in Poiseuille flow between two parallel planar solid walls

Agnieszka M. Słowicka¹, Eligiusz Wajnryb¹, and Maria L. Ekiel-Jezewska^{1a}

Institute of Fundamental Technological Research, Polish Academy of Sciences, Pawińskiego 5B, 02-106, Warsaw, Poland

August 14, 2012

Abstract. Dynamics of non-Brownian flexible fibers in Poiseuille flow between two parallel planar solid walls is evaluated from the Stokes equations, solved numerically by an accurate multipole code HYDRO-MULTIPOLE. Fibers migrate towards a critical distance from the wall z_c , which depends significantly on the fiber length N and bending stiffness A . Therefore, the calculated values of z_c can be used to sort fibers. Three modes of the dynamics are found, depending on a shear-to-bending parameter Γ . In the first mode, stiff fibers deform only a little and accumulate close to the wall, as the result of a balance between the tendency to drift away from the channel and the repulsive hydrodynamic interaction with the wall. This mechanism is confirmed by simulations in the unbounded Poiseuille flow. In the second mode, flexible fibers deform significantly and accumulate far from the wall. In both modes, the tumbling pattern is repeatable. In the third mode, the fibers are even more curved, and their tumbling is irregular.

PACS. XX.XX.XX No PACS code given

1 Introduction

Dynamics of flexible fibers in simple shear and Poiseuille flows has been analyzed theoretically, numerically and experimentally in numerous publications [1, 2, 3, 4, 5, 6, 7, 8, 9, 10, 11, 12]. Migration of fibers in Poiseuille flow [13, 14, 15, 16, 17] is the fundamental problem of modern lab-on-chip hydrodynamics, important in various biological, medical and industrial contexts, such as Brownian dynamics of proteins, actins, DNA or biological polymers, cell motion, swimming of microorganisms, drug delivery, transport of microparticles [18, 19, 20].

For significant pressure differences, corresponding to large maximal flow velocities, migration is caused by a fluid inertia [21]. However, fluid flows in microchannel devices often take place at low-Reynolds-numbers. In such systems, Brownian rigid rods migrate towards the wall [13, 14], and flexible fibers to an off-center position [22, 23, 24, 25].

For non-Brownian systems, the key question is under what conditions there exist off-center distances from microchannel walls where flexible fibers tend to accumulate, what are their values, and how they depend on the fiber size, aspect ratio and flexibility. The importance of this problem is straightforward. Focusing of micro and nanoparticles is essential for their counting, detecting, and sorting [26, 27].

The dynamics of flexible fibers is also interesting from the fundamental point of view [28]. Evolution of their non-

straight shapes is related to the existence of a family of modes, which are activated if the characteristic parameter exceeds subsequent threshold values. The parameter is determined as the ratio of the viscous forces to the bending ones [9, 10, 11, 12].

In this paper, we study both practical and fundamental aspects of the fiber dynamics. We investigate where the fibers accumulate, using the bead model and the multipole method [29] of solving the Stokes equations, implemented in a very accurate, well-tested HYDROMULTIPOLE numerical code [30]. The goal is to determine how position of accumulation planes depends on the fiber bending stiffness and its length, and to relate the findings to the characteristic parameter and its thresholds. In Sec. 2, we specify the system and theoretical model. The results are presented in Sec. 3. In Sec. 4 we conclude, discussing different modes of the fiber dynamics and thresholds of the characteristic parameter.

2 System

2.1 Fluid flow

We analyze motion and shape deformation of a single non-Brownian flexible fiber, moving freely in Poiseuille flow inside a channel made of two parallel solid walls, as illustrated in Fig. 1. The fluid velocity \mathbf{v} and pressure p satisfy the stationary Stokes equations [31, 32],

$$\eta \nabla^2 \mathbf{v} - \nabla p = \mathbf{0}, \quad \text{and} \quad \nabla \cdot \mathbf{v} = 0, \quad (1)$$

^a e-mail: mekiel@ippt.pan.pl

where η is the fluid dynamic shear viscosity.

The fluid is confined between two parallel infinite solid walls at $z = 0$ and $z = h$, with the Poiseuille flow velocity

$$\mathbf{v}_0 = 4z(h - z)/h^2 \hat{\mathbf{x}}. \quad (2)$$

The stick boundary conditions are satisfied at the surface of the fiber and at the solid walls, which confine the fluid. At infinity, the fluid velocity $\mathbf{v} = \mathbf{v}_0$.

Distances are normalized by the fiber thickness d , velocities by the maximal velocity v_m of the Poiseuille flow, forces by $f_0 = \pi\eta d v_m$, and time by $t_0 = d/v_m$.

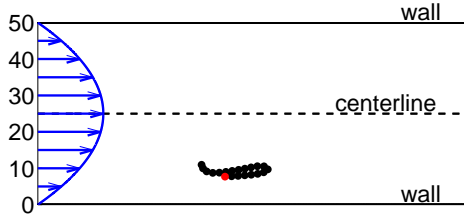


Fig. 1. A flexible fiber entrained by Poiseuille flow between two parallel solid walls.

The system defined above is important for practical applications, but complex to be studied theoretically. First, the shear rate depends on position z across the channel, and second, the hydrodynamic interaction of the fiber with the walls is significant. To separate these two effects, we also study a reference system (see Fig. 2), with the Poiseuille flow given by the same Eq. (2), but not bounded by the walls, and extending beyond $0 \leq z \leq h$.

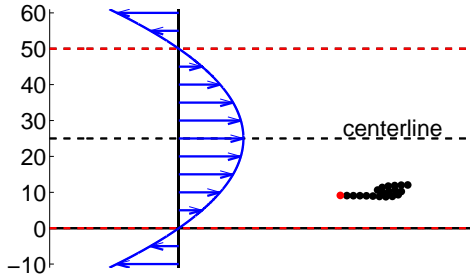


Fig. 2. Reference system: a flexible fiber entrained by unbounded Poiseuille flow (without walls).

2.2 Fiber dynamics

A single fiber consists of N solid spherical beads of diameter d equal to the fiber thickness [33]. Owing to non-hydrodynamic constraints, the beads do not move apart. There are no non-hydrodynamic torques, and the non-hydrodynamic force exerted on each bead $i = 1, \dots, N$ by its neighbors is the sum of the elastic and bending forces [18],

$\mathbf{F}_i = \mathbf{F}_i^e + \mathbf{F}_i^b$, with

$$\mathbf{F}_i^e = -k(l_i - l_0)\hat{\mathbf{t}}_i + k(l_{i+1} - l_0)\hat{\mathbf{t}}_{i+1}, \quad (3)$$

$$\mathbf{F}_i^b = -\frac{A}{2l_0}\nabla_i \sum_{n=2}^{N-1} (\hat{\mathbf{t}}_{n+1} - \hat{\mathbf{t}}_n)^2, \quad (4)$$

where k is the ratio of the Hooke's constant to f_0 and A is the ratio of the bending stiffness to $f_0 d^2$ (in the following just called the bending stiffness). In the above equation, l_0 and l_i denote the equilibrium and time-dependent distances between the centers of the consecutive beads, respectively, with $l_i = |\mathbf{t}_i|$, where $\mathbf{t}_i = \mathbf{r}_i - \mathbf{r}_{i-1}$ is the difference between the positions \mathbf{r}_k of the consecutive bead centers $k = i - 1, i$. Here, $\hat{\mathbf{t}}_i = \mathbf{t}_i/l_i$ and ∇_i is the derivative with respect to \mathbf{r}_i . The total non-hydrodynamic force applied to all the fiber beads vanishes, $\sum_{i=1}^N \mathbf{F}_i = 0$.

Translational and rotational velocities of the fiber beads, $\mathbf{U} = (\mathbf{U}_1, \dots, \mathbf{U}_N)$ and $\mathbf{\Omega} = (\mathbf{\Omega}_1, \dots, \mathbf{\Omega}_N)$, are linear combinations of the non-hydrodynamic forces $\mathbf{F} = (\mathbf{F}_1, \dots, \mathbf{F}_N)$ exerted on them all, and the multipoles of the ambient velocity field (2), with the coefficients determined by the elements of the grand mobility matrix [34]. All the terms related to the ambient flow can be interpreted as resulting from the hydrodynamic forces $\mathbf{F}_0 = (\mathbf{F}_{01}, \dots, \mathbf{F}_{0N})$ and torques $\mathbf{T}_0 = (\mathbf{T}_{01}, \dots, \mathbf{T}_{0N})$, exerted by the same ambient flow (2) on motionless beads fixed at the same instantaneous positions as the fiber beads,

$$\begin{pmatrix} \mathbf{U} \\ \mathbf{\Omega} \end{pmatrix} = \boldsymbol{\mu} \cdot \begin{pmatrix} \mathbf{F} + \mathbf{F}_0 \\ \mathbf{T}_0 \end{pmatrix}, \quad (5)$$

with the mobility matrix $\boldsymbol{\mu}$ dependent on the instantaneous positions of all the bead centers, $\mathbf{r} = (\mathbf{r}_1, \dots, \mathbf{r}_N)$.

For a given configuration, values of \mathbf{F}_0 , \mathbf{T}_0 and $\boldsymbol{\mu}$ are determined by the multipole expansion of the Stokes equations [29, 35], with the wall effects evaluated by the single-wall superposition [36, 37]. The computations are performed with the use of the HYDROMULTIPOLE numerical code [30]. Then, the adaptive fourth-order Runge-Kutta method is applied to determine the fiber dynamics,

$$d\mathbf{r}/dt = \mathbf{U}. \quad (6)$$

Initially, the fiber is aligned with the flow (i.e. along the x axis), with the bead centers located at $\mathbf{r}_i = (il_0, 0, z_0)$, for $i = 1, \dots, N$. Owing to symmetry, the fiber moves in the xz plane. The computations are three-dimensional, and no deformation of the fiber out of the plane is observed.

2.3 Parameters

In the numerical simulations, we have used single values of the bead diameter (length unit), the channel width h , the Hooke's constant k and the equilibrium distance between the consecutive beads l_0 ,

$$h = 50, \quad k = 80, \quad l_0 = 1.01. \quad (7)$$

A large value of k and small gap size ($l_0 - 1$) between the beads are chosen to model compact fibers which practically do not change their length while bending.

Three values of the fiber length N (in our units equal to the number of beads, or the aspect ratio) have been considered, with the corresponding fraction of the channel width, $L = N/h$, explicitly given in Table 1. For clarity of presentation, we focus on discussing in details the results obtained for $N = 10$.

Table 1. The fiber length $L = N/h$ as a fraction of the channel width for the fiber aspect ratio N used in the simulations.

N	5	10	20
L	0.1	0.2	0.4

Computations have been performed for a wide range of the initial fiber positions z_0 across the channel. The values of the bending stiffness A ranged from $0.01 \leq A \leq 2$, and have been chosen to observe thresholds for different modes of the dynamics. It is known [9, 10, 11, 12] that the transitions between C, S and W modes are associated with specific values of a dimensionless parameter, equal to the ratio of the viscous forces (proportional to the local shear rate) to the bending ones. This parameter is widely used to characterize systems, which are far from interfaces. However, it is clear that under confinement (as in the system

considered in this work), there are additional wall effects which may influence thresholds of the fiber dynamics. In this paper, we are going to study these effects, by comparing our system (Fig. 1) with the reference one (Fig. 2). We use two basic parameters N and A to describe the fiber evolution. For $N = 10$, we evaluate a simple shear-to-bending dimensionless number mentioned above,

$$\Gamma = (h/2 - z_m)/A, \quad (8)$$

and analyze its critical values at the thresholds, and their dependence on the distance z_m from the fiber center-of-mass to the closer wall.

3 Results

3.1 Lateral migration and accumulation planes

In Ref. [38], dynamics of fibers in the same system was analyzed, focusing on the migration towards the central plane of the channel and its dependence on the fiber stiffness, aspect ratio and distance from the wall [38]. But for certain values of these parameters, fibers migrate away from the central plane. In this paper, we determine the critical distance z_c from the wall where fibers accumulate.

Fig. 3 shows evolution of the distance $z_m(t)$ between the fiber center-of-mass and the closer wall, starting from

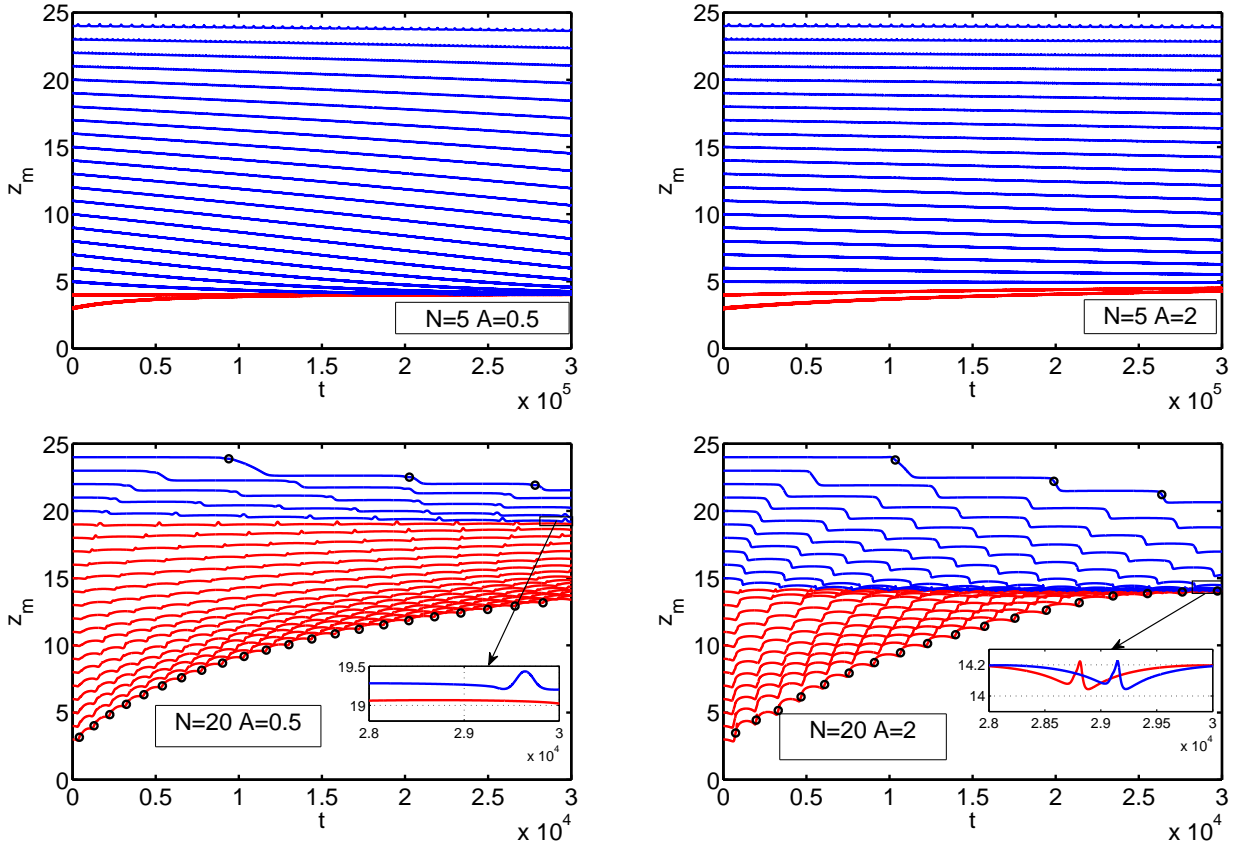


Fig. 3. Evolution of the distance $z_m(t)$ from the fiber center-of-mass to the wall, for fibers initially aligned with the flow. Here, $z=0$ and $z=25$ correspond to the wall and the central plane of the channel, respectively. Black circles denote flipping instants.

Table 2. The distance z_c from the wall where fibers accumulate.

$N \backslash A$	0.025	0.05	0.125	0.2	0.25	0.38	0.46	0.5	1.0	2.0
5	16.81	9.11	4.48	4.3	4.19			4.02	4.3	4.7
	3.6									
	(± 0.1)	(± 0.05)	(± 0.02)	(± 0.1)	(± 0.02)			(± 0.05)	(± 0.1)	(± 0.1)
10		22.2	19.33	14.45	12.4	8.9	8.3	8.2	7.5	6.4
		10.1								
		(± 0.1)	(± 0.05)	(± 0.05)	(± 0.2)			(± 0.1)	(± 0.1)	(± 0.1)
20					21.28			19.1	15.9	14.2
					(± 0.1)			(± 0.2)	(± 0.1)	(± 0.1)

different values $z_m(0) = z_0$. Online, positions of the fibers, which move towards (away from) the central plane of the channel are plotted in red (blue).

All fibers tend to an off-center position across the flow. For $N = 5$, the migration rate is significantly slower than for $N = 20$ (notice the 10 times larger range of times of the upper plots in Fig. 3).

The lateral migration of fibers is superimposed with oscillations of their center-of-mass position, clearly visible in Fig. 3 for $N = 20$. These oscillations are related to the fiber tumbling motion, caused by the local shear of the flow. A flipping time t_f is defined as the instant when the end-to-end vector (which links the centers of the first and the last beads of the fiber) becomes perpendicular to the flow direction. The distance from the fiber center-of-mass to the wall at time t_f will be denoted as z_f ,

$$z_f \equiv z_m(t_f). \quad (9)$$

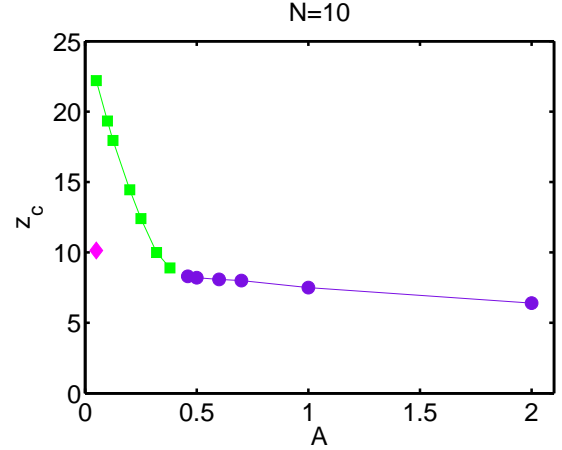
In Fig. 3, consecutive positions z_f are marked at four selected simulation runs with $N = 20$.

For all fibers, z_f tends to a critical position z_c ,

$$z_f \longrightarrow z_c \quad \text{when} \quad t \longrightarrow \infty. \quad (10)$$

The value of z_c depends on the fiber aspect ratio N , and the fiber stiffness A . Some of the evaluated values of z_c are listed in Table 2. Their relative accuracy (typically, 0.5-2%), is determined as the maximum of the oscillation amplitude and the half-a-distance between the closest decreasing and increasing curves $z_m(t_f)$, at the last flipping instant t_f observed in our simulations.

For $N = 10$, the results are shown in Fig. 4. For larger values of A , the accumulation plane is located at

**Fig. 4.** Position z_c of the accumulation plane versus the fiber bending stiffness A , for $N = 10$.

the position z_c larger than half of the fiber length, $N/2$, but smaller than N (circles, violet online). However, for a smaller values of A , the accumulation distance rapidly increases with the decreasing A (squares, green online). When z_c becomes sufficiently close to the mid-plane of the channel, the second accumulation plane is observed for the same value of A (diamond, magenta online). For $N = 5$ and $N = 20$, a similar tendency is visible in Table 2.

It seems that accumulation of stiff fibers is caused by the wall, which prevents them from escaping. Flexible fibers, however, accumulate far from the wall, probably owing to their shape deformation and the flow curvature. This hypothesis will be verified in the next section.

Table 3. The position $z_c^{\text{no-wall}}$ where fibers accumulate in the absence of walls. The arrows \searrow indicate that there is no accumulation position - all fibers migrate away towards $z_m < 0$.

$N \backslash A$	0.025	0.05	0.125	0.2	0.25	0.38	0.46	0.5	2.0
5	16.8	8.65	\searrow	\searrow	\searrow			\searrow	\searrow
	(± 0.1)	(± 0.1)							
10		22.2	17.85	14.2	11.75	5.49	\searrow	\searrow	\searrow
		5.8							
		(± 0.1)	(± 0.05)	(± 0.1)	(± 0.05)				
20								18.6	2.6
								(± 0.1)	(± 0.1)

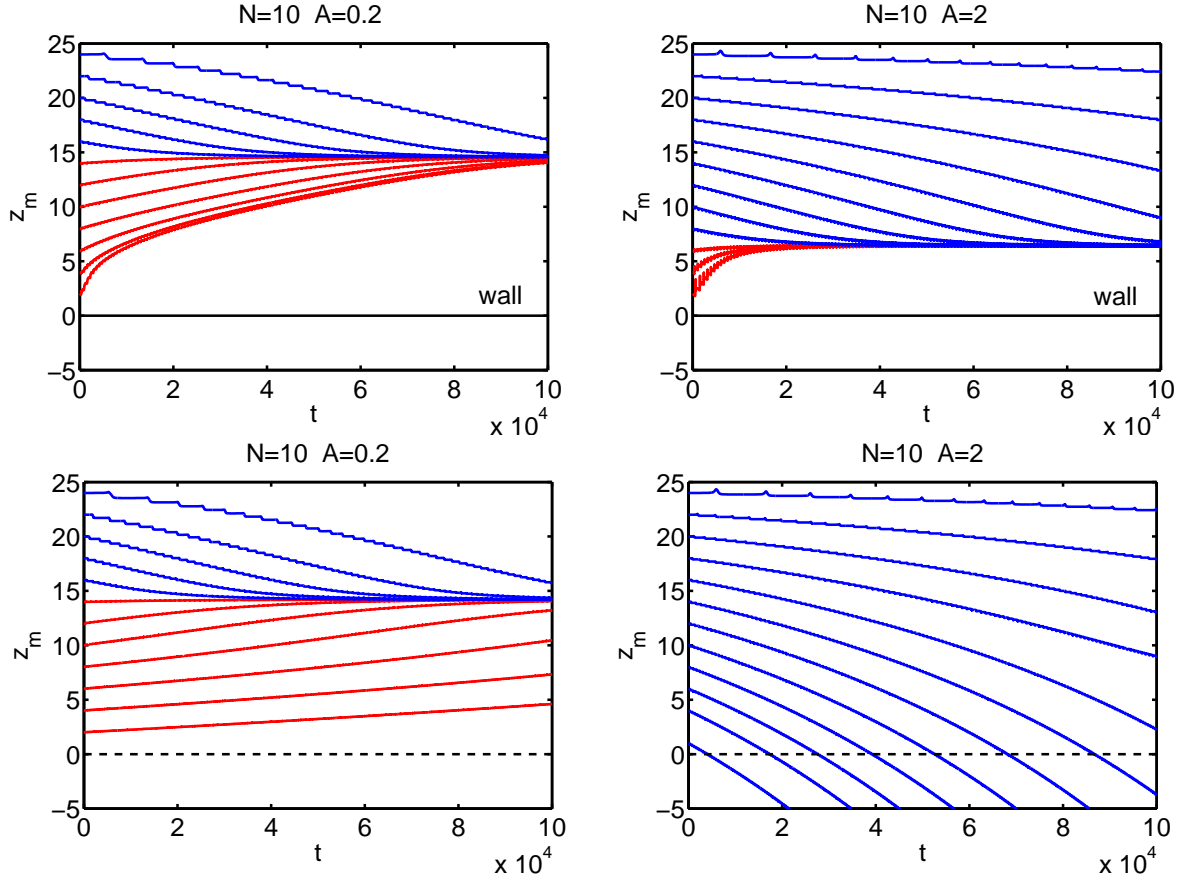


Fig. 5. Evolution of the distance $z_m(t)$ from a fiber center-of-mass to the closer plane, where the ambient Poiseuille flow vanishes. Top: the flow bounded by the walls, as in Fig. 1. Down: the same fiber and the flow, but without walls, as in Fig. 2.

3.2 Comparison with unbounded Poiseuille flow helps to discriminate between two modes of accumulation

In Table 3, we evaluate positions $z_c^{\text{no-wall}}$ of the accumulation planes for the same fibers and the same ambient flow as in the previous section, but without walls (the system shown in Fig. 2). For more flexible fibers, the accumulation planes are located in approximately the same position with and without the walls, $z_c \approx z_c^{\text{no-wall}}$, see the left panels of Fig. 5 ($N = 10$ and $A = 0.2$). However, the motion of more stiff fibers significantly depends on the presence or absence of the walls. The difference can be seen by comparing the top and bottom right panels of Fig. 5 ($N = 10$ and $A = 2$). With walls, the fibers accumulate at $z_f = z_c$ inside the channel. Without walls, the fibers migrate out of the “channel regime” (defined as $0 \leq z_f \leq h$), whatever is their initial position across the flow; there is no accumulation points in this range of z_f . In Table 3, such a behavior is indicated by arrows pointing down-right.

Clearly, there exist two modes of the fiber accumulation inside the channel: caused by its hydrodynamic interaction with the wall (violet circles in Fig. 4, $\Gamma < 36$) and caused by its interaction with the flow itself (green squares in Fig. 4, $\Gamma > 42$), where the parameter Γ is defined by Eq. (8), with the center-of-mass (always in this paper) taken at the flipping instant, $z_m \equiv z_f$. The tran-

sition between both modes takes place for a critical value Γ_0 such that

$$36 \leq \Gamma_0 \leq 42. \quad (11)$$

In the next section, we will investigate if the transition between both accumulation modes is correlated with a change of fiber shapes.

3.3 Fiber shapes

In Fig. 6, we compare evolution of fiber shapes for both modes. The snapshots are labeled by the corresponding values of the rescaled time, \bar{t}/τ , defined by the relations,

$$\bar{t} = t - t_f(2), \quad (12)$$

$$\tau = t_f(3) - t_f(2), \quad (13)$$

where $t_f(n)$ is the instant of the n -th flip. The indicated fiber position z_f corresponds to the second flipping instant $t_f(2)$ (i.e. to $\bar{t} = 0$).

In the top panel of Fig. 6, $A = 0.2$, and in the bottom one, $A = 1$. We first compare the snapshots taken at two critical positions z_c from different accumulation modes. The first mode (accumulation caused by the walls, smaller Γ , violet color online), seen in the middle row of the top panel, corresponds to the S-shaped type of the motion. The second mode (accumulation independent of the walls, larger Γ , green color online), shown in the middle row of the bottom panel, is only slightly bended.

To quantify this difference, we introduce two parameters of a fiber shape: the curvature κ (as in Ref. [11]) and the fractional compression α (as in Ref. [12]). The time-dependent fiber curvature,

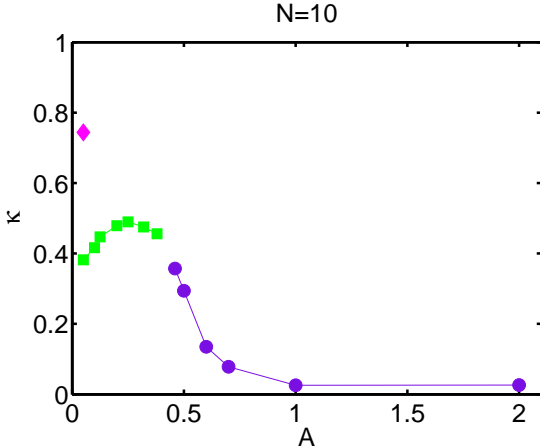


Fig. 7. The fiber curvature κ at the instant of flipping at the accumulation plane z_c , versus its bending stiffness A .

$$\kappa = \frac{1}{N-2} \sum_{i=2}^{N-1} \frac{1}{r_i}, \quad (14)$$

is defined as the mean inverse radius $1/r_i$ of the circle determined by the centers of three consecutive beads.

In Fig. 7, we present values of κ for fibers made of $N = 10$ beads, with the center-of-mass at the accumulation plane z_c at the flipping instant t_f .

The fiber fractional compression is defined as [12]

$$\alpha = 1 - \delta(t_f)/N, \quad (15)$$

where $\delta(t_f)$ is the end-to-end distance of the fiber located at the accumulation distance z_c in the time of flipping t_f .

(The end-to-end distance means the distance between the centers of the first and the last bead.)

In Fig. 8, we present values of α for fibers made of $N = 10$ beads, with the center-of-mass at the accumulation plane z_c at the flipping instant t_f .

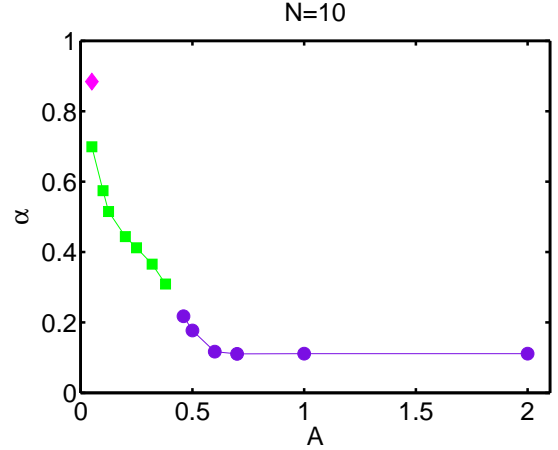


Fig. 8. The fiber fractional compression α , defined in Eq. (15), at the flipping instant t_f and distance z_c , versus its bending stiffness A .

From Figs. 7 and 8, it is evident that for the second accumulation mode ($A < 0.38$, green squares), both the curvature and the fractional compression of the fibers flipping at the accumulation distance z_c are much higher than for the first one ($A > 0.46$, violet circles), with the rapid change in the transition range, in agreement with the previous analysis of the corresponding snapshots in Fig. 6.

Until now, we have discussed the modes of the fiber dynamics only at the accumulation trajectories. In Figure 6, the fiber shapes at other trajectories are also shown. Eqs. (8) and (11) are now used to determine values of the parameter Γ for each trajectory. It is interesting that for $\Gamma < \Gamma_0$ (the rows 1, 4, 5 and 6), the C-shaped type of motion is observed, and for $\Gamma > \Gamma_0$ (the rows 2 and 3) - the S-shaped one. Such a transition to shape instability, triggered by a critical value of the shear-to-bending number (equivalent to our Γ_0) is known in the literature, see [9,12] and the references within.

3.4 Third (irregular) mode of the fiber dynamics

In the previous sections, only two modes of the fiber dynamics have been discussed. However, in Figs. 7 and 8, for a very small value of the bending stiffness $A = 0.05$, there appear also an accumulation plane (diamond, magenta online), which corresponds to much higher curvature and fractional conversion than the other ones. The corresponding (very compact) fiber shapes are shown in the lowest row of Fig. 9. From Fig. 4 it is clear that this plane is much closer to the wall than the accumulation planes of the second (green) type. Moreover, it is one of



Fig. 6. Evolution of a fiber shape (drawn to scale) for $N = 10$. Up: $A = 0.2$. Down: $A = 1$. Snapshots from simulations taken at the indicated times \bar{t}/τ (with $\bar{t} = t - t_f(2)$ and $\tau = t_f(3) - t_f(2)$, where $t_f(n)$ is the instant of the n -th flip). The indicated values of z_f are attained at $\bar{t} = 0$ (second flip).

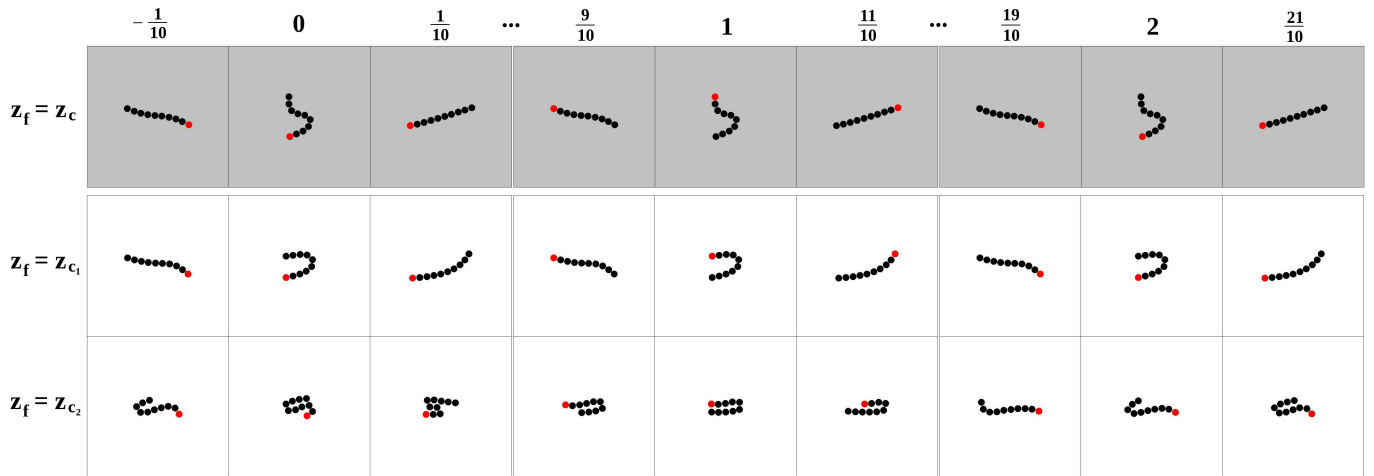


Fig. 9. Evolution of a fiber shape (drawn to scale) for $N = 10$. Top: $A = 0.2$ and $z_c = 14.45$. Middle: $A = 0.05$ and $z_{c_1} = 22.2$. Bottom: $A = 0.05$ and $z_{c_2} = 10.1$. Snapshots from simulations are taken at the indicated values of the time \bar{t}/τ , defined by Eqs. (12)-(13). Zero and one correspond to the consecutive flipping instants.

two accumulation planes observed for the same value of the bending stiffness $A = 0.05$. The migration to these two planes is shown in Fig. 10, with the accumulation distances $z_c = 10.1$ for the third, and $z_c = 22.2$ for the second mode.

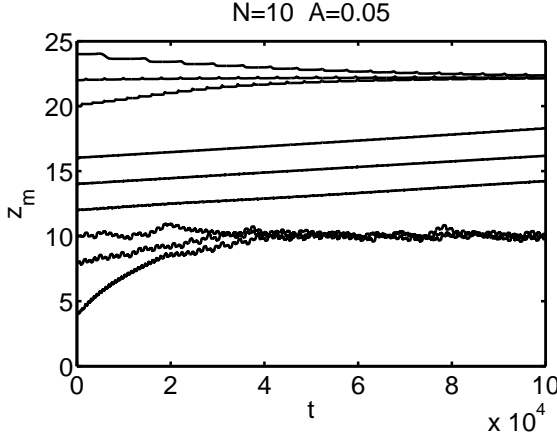


Fig. 10. Evolution of the distance $z_m(t)$ from the fiber center-of-mass to the wall, for $N = 10$ and $A = 0.05$. The lower accumulation plane corresponds to the third mode, and the upper one to the second mode.

The essential difference between trajectories corresponding to both modes is their time-dependence: regular for the second, and irregular for the third mode. This effect is visible in Fig. 10 as small irregular fluctuations of the lower trajectories. This property can be used to determine the critical value Γ_1 of the parameter Γ at the transition between these two modes,

$$260 < \Gamma_1 < 298. \quad (16)$$

To study the nature of the irregular behavior, in Fig. 9 we compare evolution of shapes. At the trajectories of the second type (top and middle panels)¹, fibers bend in a repeatable way, changing pattern almost periodically, with the half-period determined by the tumbling time τ between consecutive flips, which occur at integer values of \bar{t}/τ , c.f. Eqs. (12)-(13) for the notation. In contrast, the shapes of fibers at the third mode (bottom row) are not repeatable.

In Fig. 11, we study time dependence of the fiber curvature. Colors visible online mark different modes of the fiber dynamics. For a fiber motion of the second mode (dashed curve, $\Gamma \approx 53$), κ is almost perfectly periodic. The solid curve corresponds to the fiber shapes shown in the bottom row of Fig. 9, with $\Gamma \approx 298$ (the third mode), and it is quasi-periodic (but not regular). The dashed-dotted

¹ Notice that the fiber evolution shown in the top panel of Fig. 9, with $\Gamma \approx 53$, is S-shaped, but in the middle panel, where $\Gamma \approx 56$, it is C-shaped. This example indicates that there is no universal correlation between the value of Γ and the shape type. This might be related to the value of $z_c = 22.2$ very close to the middle plane of the channel, or other reasons.

curve, with even larger value $\Gamma \approx 900$, is completely irregular.

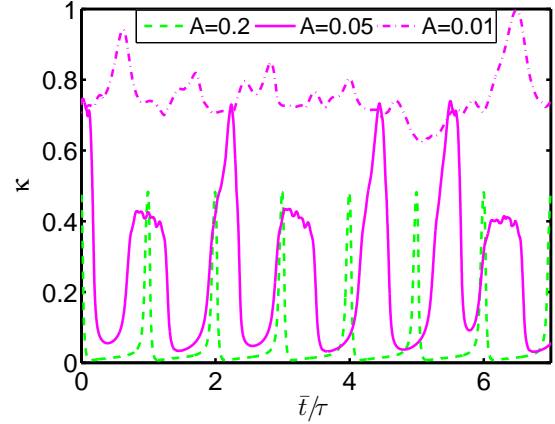


Fig. 11. The time-dependent curvature κ of fibers with $N = 10$ moving at z_m . Dashed line (green online): $z_m \approx z_f = 14.45$ and $A = 0.2$. Solid line (magenta online): $z_m \approx z_f = 10.1$ and $A = 0.05$. Dashed-dotted line (magenta online): $z_m \approx 16$ and $A = 0.01$. The reduced time \bar{t}/τ is defined by Eqs. (12)-(13).

3.5 Tumbling time

It is interesting to determine how tumbling of fibers depends on their position across the channel. In Fig. 12, the fiber flipping frequency $1/\tau$ is plotted as a function of the distance z_f from the wall at the flipping instant. For the first and the second modes, it is a monotonically decreasing function (except fibers, which are close to the wall). Fibers at a larger distance from the wall tumble at a slower rate. Short fibers tumble more frequently in comparison to long fibers (notice a different scale on vertical axis of each panel in Fig. 12). Both effects are significant. The tumbling frequency is a bit larger for a smaller bending stiffness A . The difference is more pronounced for longer fibers.

Following the idea of Bretherton [39], widely used in various contexts [1,2], we are now comparing the tumbling time τ characteristic for our flexible fibers entrained by the Poiseuille flow between two walls with the classic result of Jeffrey for the rotation half-period $T/2$ of rigid ellipsoids of revolution immersed in a simple shear flow in an unbounded fluid [40]. Jeffrey derived the following relation between the rotation frequency $2/T$ and the shear rate $\dot{\gamma}$,

$$\frac{2}{T} = \frac{\dot{\gamma}}{\pi(r_e + 1/r_e)}, \quad (17)$$

where r_e is the aspect ratio for the ellipsoid of revolution.

For the Poiseuille flow, the shear rate depends on the position z across the channel,

$$\dot{\gamma}(z) = 8(h/2 - z)/h^2, \quad (18)$$

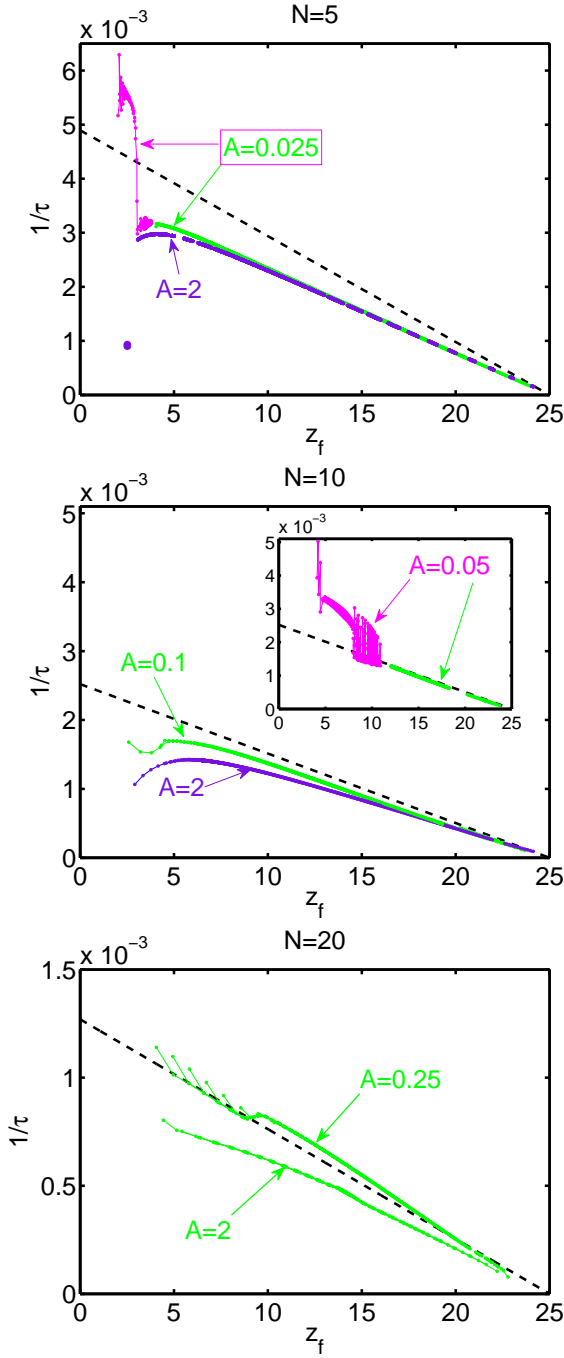


Fig. 12. The fiber tumbling frequency $1/\tau$ versus its distance z_f from the wall (solid lines), in comparison to the inverse half-period of a rigid spheroid with the aspect ratio N (Jeffrey, dashed line). Top: $N=5$. Middle: $N=10$. Bottom: $N=20$.

where, in our case, the channel width $h = 50$.

In Fig. 12, we compare our numerical results for the tumbling frequency of flexible fibers, $1/\tau$, plotted as a function of z_f (solid lines), with the Jeffrey's linear relation $\dot{\gamma}(z_f)/\pi(r_e + 1/r_e)$, which follows from Eqs. (17)-(18). In general, an agreement would be expected for an effective

value of r_e . As the reference, we plot the dashed line, which corresponds just to $r_e = N$.

From Fig. 12 it follows that for larger distances from the wall, $1/\tau$ is indeed proportional to $(h/2 - z_f)$. The surprising effect is that the slope is quite well-approximated assuming that the effective hydrodynamic aspect ratio r_e of flexible fibers is just equal to the number of beads N ,

$$r_e = N. \quad (19)$$

Unexpectedly, a better agreement is observed for longer and more flexible fibers which deform significantly during the tumbling, with the average geometrical aspect ratio much smaller than N .

For smaller distances from the wall, it is known from the literature that the Jeffrey approximation is not sufficient owing to the hydrodynamic interaction between the fiber and the wall, see Fig. 5 in Ref. [2].

The above discussion has been performed for the first and second mode of the dynamics (violet and green curves online). The third mode (magenta online) is seen in Fig. 12 as non-smooth, rapidly fluctuating lines, what reflects well the nature of this irregular mode.

4 Conclusions

In this work, we have considered dynamics of fibers, which are immersed in a low-Reynolds-number Poiseuille flow between two parallel planar solid walls at $z = 0$ and $z = h$, and are initially aligned with the flow. Our key finding is that fibers with a different length (i.e. a different number of segments N) and a different ratio A of the bending stiffness to the flow amplitude, tend to accumulate at a different critical distance z_c from the wall. The differences are pronounced. The dependence of z_c on A and N has been determined numerically in a wide range of the parameters, based on more than 400 simulation runs.

There exist two different mechanisms of the fiber accumulation. For stiff fibers, hydrodynamic interaction with the close wall prevents them from drifting out of the channel. Therefore, in this case z_c is a bit more than half of the fiber length N , but still less than N . This mechanism of the accumulation has been confirmed by the simulations performed for the same fiber and the same Poiseuille flow inside the channel range $0 < z < h$, but in the absence of walls. Without walls, stiff fibers migrate away from the channel range $0 < z < h$, whatever the initial position is. In contrast, flexible fibers tend to accumulate at larger distances $z_c > N$, with similar values in the presence and in the absence of the walls. In this case, the accumulation mechanism is an interplay of the flow curvature, the fiber length and the fiber bending stiffness.

The comparison with the unbounded flow was used as the criterion to discriminate between two different modes of the fiber dynamics. The additional differences between these two modes are the following. The first one has a larger fiber curvature and a larger fractional conversion. A correlation of the first mode with the C-shaped type of the motion, and of the second mode with the S-shaped

type of the motion has been observed for some cases. This problem will be studied in details elsewhere.

A third mode has been also detected. Its basic feature (used to distinguish it from the second mode) is the irregular time dependence, best visible while analyzing the tumbling time, see Fig. 12. In addition, for the third mode the fiber curvature and its fractional conversion are much larger than for the second mode.

Our findings agree well with the previous literature related to the fiber transitions to higher modes [9, 10, 11, 12, 28]. Following these papers, for $N = 10$ we have determined values of a shear-to-bending parameter $\Gamma = (h/2 - z_f)/A$, and found its thresholds Γ_0 and Γ_1 for the transitions between the successive modes. Our findings are illustrated in Fig. 13. Similar analysis has been (or can be) performed for other values of the fiber length N . This will be done in a next paper.

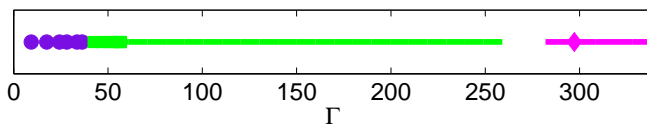


Fig. 13. Values of the shear-to-bending parameter Γ for $N=10$. Three modes (different colors online) are separated by the thresholds $\Gamma_0=36$ and $\Gamma_1=260$.

The results presented in this work can be used to sort non-Brownian flexible microfibers, depending on their length and bending stiffness. To this goal, additional measurement of their bending stiffness A is necessary. The analysis presented here indicates that neither the shape evolution nor the tumbling time is sufficient to determine specific value of A .

Time and length scales of a fiber migration are relatively large. For example, in a microchannel of width $h = 250 \mu\text{m}$, with the maximal Poiseuille flow velocity $v_m = 1 \text{ mm/s}$, a fiber of thickness $5 \mu\text{m}$ and length $100 \mu\text{m}$, initially located at the distance $h/4$ from the wall, typically approaches a distance close to z_c after 60 – 300 seconds, translating by 50 – 200 mm.

Acknowledgments

We thank Professor Jerzy Bławdziewicz for insightful discussions. This work was supported in part by the Polish Ministry of Science under grant 2011/01/B/ST3/05691.

References

1. Yamamoto S. and Matsuoka T., J. Chem. Phys. **198** (1993), 644.
2. Zurita-Gotor M., Bławdziewicz J. and Wajnryb E., J. Rheol. **51** (2006), 71.
3. Lindstrom S. B. and Uesaka T., Phys. Fluids **19** (2007), 113307.
4. Usta O. B., Butler J. E. and Ladd A. J. C., Phys. Rev. Lett. **98** (2007), 098301.
5. Winkler R. G., J. Chem. Phys. **133** (2010), 164905.
6. Huang C.-C., Winkler R. G., Sutmann G. and Gompper G., Macromolecules **43** (2010), 10107.
7. Ladd A. J. C., Kekre R. and Butler J. E., Phys. Rev. E **82** (2010), 050803.
8. Huang C.-C., Sutmann G., Gompper G. and Winkler R. G., EuroPhys. Lett. **93** (2011), 54004.
9. Becker L. E., Shelley M. J., Phys. Rev. Lett. **87** (2001), 198301.
10. Young Y.-N., Shelley M. J., Phys. Rev. Lett. **99** (2007), 058303.
11. Wandersman E., Quennou N., Fermigier M., Lindner A. and du Roure O., Soft Matter **6** (2010), 5715.
12. Kantsler V. and Goldstein R. E., Phys. Rev. Lett. **108** (2012), 038103.
13. Nitsche L. C. and Hinch E. J., J. Fluid Mech. **332** (1997), 1.
14. Schiek R. L. and Shaqfeh E. S., J. Fluid Mech. **332** (1997), 23.
15. Usta O. B., Butler J. E. and Ladd A. J. C., Phys. Fluids **18** (2006), 031703.
16. Chelakkot R., Winkler R. G. and Gompper G., EuroPhys. Lett. **91** (2010), 14001.
17. Reddig S. and Stark H., J. Chem. Phys. **135** (2011), 165101.
18. Gauger E. and Stark H., Phys. Rev. E **74** (2006), 021907.
19. Tornberg A.-K. and Shelley M. J., J. Comp. Phys. **196** (2004), 8.
20. Sadlej K., Wajnryb E., Ekiel-Jezewska M. L., Lamparska D. and Kowalewski T. A., Int. J. Heat Fluid Fl. **31** (2010), 996.
21. Segré G. and Silberberg A., Nature **189** (1961), 209.
22. Usta O. B., Ladd A. J. C. and Butler J. E., J. Chem. Phys. **122** (2005), 094902.
23. Winkler R. G., Phys. Rev. Lett. **97** (2006), 128301.
24. Cannavacciuolo L., Winkler R. G. and Gompper G., EuroPhys. Lett. **83** (2008), 34007.
25. Kekre R., Butler J. E. and Ladd A. J. C., Phys. Rev. E **82** (2010), 011802.
26. Xuan X., Zhu J. and Church C., Microfluidics and Nanofluidics **9** (2010), 1.
27. Kim Y. and Yoo J., Optics and Lasers in Engineering **50** (2012), 87.
28. de Gennes P. G., J. Chem. Phys. **60** (1974), 5030.
29. Cichocki B., Felderhof B. U., Hinsen K., Wajnryb E. and Bławdziewicz J., J. Chem. Phys. **100** (1994), 3780.
30. Cichocki B., Ekiel-Jezewska M. L. and Wajnryb E., J. Chem. Phys. **111** (1999), 3265.
31. Kim S. and Karrila S. J. *Microhydrodynamics. Principles and Selected Applications* (Dover Publications, Mineola) 2005.
32. Happel J. and Brenner H., *Low Reynolds Number Hydrodynamics* (Nordhoff International Publishing, Leyden) 1973.
33. Dhont J. K. and Briels W., *Rod-like Brownian Particles in Shear Flow* (WILEY-VCH Verlag, Berlin) 1988.
34. Felderhof, B. U., Physica A **151** (1988), 1.
35. Ekiel-Jezewska M. L. and Wajnryb E., in: *Theoretical Methods for Micro Scale Viscous Flows* (F. Feuillebois and A. Sellier, eds., Transworld Research Network, Kerala) 2009.

36. Cichocki B., Jones R., Kutteh R. and Wajnryb E., J. Chem. Phys. **112** (2000), 2548.
37. Bhattacharya S., Bławdziewicz J. and Wajnryb E., Physica A **356** (2005), 294.
38. Słowicka A., Ekiel-Jeżewska M., Sadlej K. and Wajnryb E., J.Chem.Phys. **136** 2011, 044904.
39. Bretherton F., J. Fluid Mech. **14** (1962), 284.
40. Jeffery G., Proc.R.Soc. **102** (1922), 161.